

# Experimental study of single- and double-electron transfer in slow $\text{Ne}^{8+} + \text{He}$ collisions using photon and electron spectroscopy

A. Langereis and J. Nordgren

*Department of Physics, Uppsala University, Box 530, S-751 21 Uppsala, Sweden*

S. Bliman

*Université de Marne la Vallée, Allée Jean Renoir, F-93160, Noisy le Grand, France*

M. Cornille

*DARC Observatoire de Paris, UPR 176 CNRS, 92195 Meudon, France*

R. Bruch and R. A. Phaneuf

*Department of Physics, University of Nevada, Reno, Nevada 89557*

D. Schneider

*Lawrence Livermore Laboratory, P.O. Box 808, Livermore, California 94550*

(Received 22 January 1999)

Single- and double-electron transfer from He to the  $\text{Ne}^{8+}(1s^2)S_0^1$  ion has been studied at 80 keV by extreme ultraviolet (EUV) spectroscopy and zero-degree electron spectroscopy. Signals originating from the stabilization after two-electron capture are identified in the photon data. This gives information on the stabilization of two electrons on the projectile. Single-electron capture signals originating from  $n=9$  states are observed, and the absolute emission cross section is determined. The presented experimental data have unprecedented resolution. The analysis is supported by extensive theoretical calculations of the (3,3), (3,4), and (4,4) doubly excited states in Be-like neon. Decay from triplet states due to spin exchange is observed in the spectra. [S1050-2947(99)09809-1]

PACS number(s): 34.70.+e

## I. INTRODUCTION

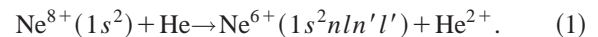
Single-electron transfer processes (SC) in slow collisions between highly charged ions and neutral atoms have been studied intensively during the last two decades. It is generally recognized that these processes are well understood apart from the detailed collision dynamics, such as the population mechanism for  $l$  quantum states. Therefore, most interest has shifted to multiple-electron-capture processes (DC) during the last years [1].

The  $\text{Ne}^{8+} + \text{He}$  collision system has received much attention in this context, and several authors have reported on theory and experiments. Electron spectroscopy has been used most often to investigate the collision dynamics and the decay of doubly excited states populated in two-electron transfer processes. An analysis of this collision system has been done by Boudjema *et al.*, [2,3] where also references to previous work can be found. Photon spectroscopy is not often used, since the doubly excited states populated in the double electron transfer processes mainly stabilize by Auger decay. This technique also has an inherent inefficiency due to the small solid angle subtended ( $\approx 2 \times 10^{-5}$  sr) if a resolution comparable to the typical resolution obtained with electron spectroscopy is needed. Additionally, detectors in the soft-x-ray region are relatively inefficient. Photon spectroscopic data has been recorded previously, but mainly SC processes [4–6] were studied. The one experimental work that discussed DC processes suffered from poor resolution in the recorded data set [7].

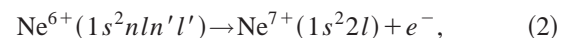
In this paper we report on spectroscopic observations of the  $\text{Ne}^{8+} + \text{He}$  collision system at an impact energy of 4.0 keV  $\text{amu}^{-1}$  performed by high-resolution soft-x-ray emission spectroscopy in the 60–140-Å wavelength range and zero-degree electron spectroscopy. Both data sets were recorded under identical experimental conditions, except for the observation angle under which the reaction products were observed.

Recent advances of highly charged ion sources have opened up new experimental possibilities for high-resolution spectroscopic observations [8]. The resolution of the spectroscopic data presented in this paper is unprecedented, to our knowledge, and enables us to study radiative and nonradiative decay with high precision.

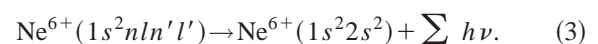
Two-electron transfer processes in slow ion-atom collisions result in high-lying projectile doubly excited states ( $n, n'$ ), usually lying above the ionization limit, Eq. (1):



These states can stabilize by Auger electron decay, which is often called autoionizing double capture (ADC) [Eq. (2)]



or by stabilizing both electrons on the projectile; this is often called “true” double capture (TDC) [Eq. (3)].



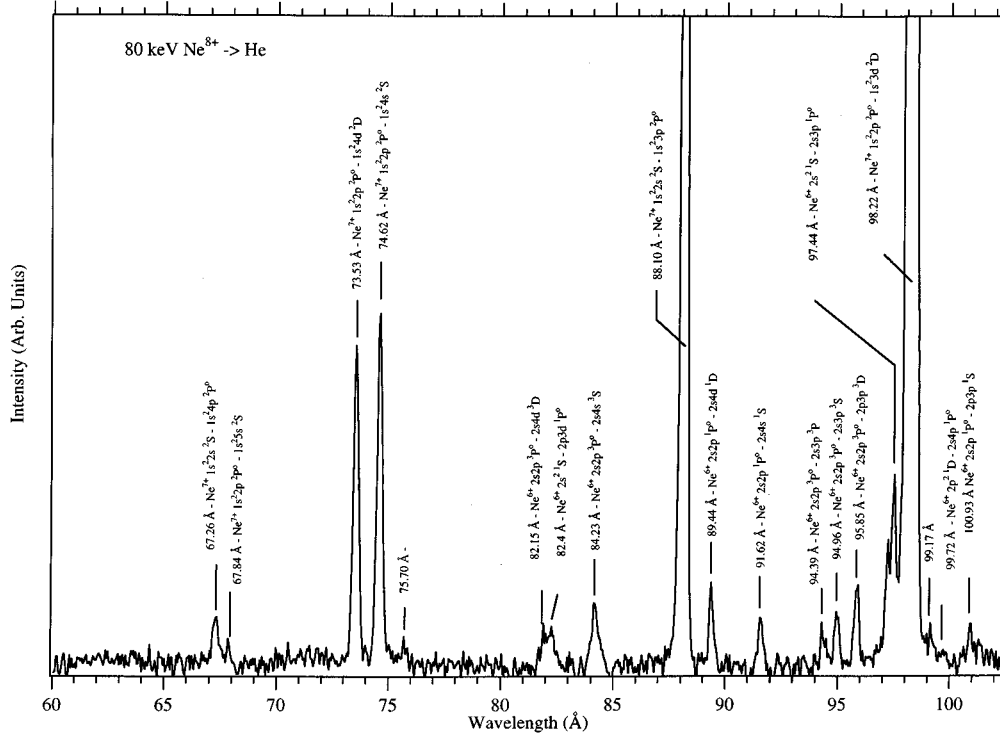


FIG. 1. EUV spectrum, 60–102.5 Å, resulting from 4.0-keV  $\text{amu}^{-1} \text{Ne}^{8+} + \text{He}$  collisions. The most intense lines are identified as Li-like SC channels. Most other lines are attributed to TDC decay channels. Transitions with their assignments are shown in Tables I and II. The spectrum is blown up vertically to give a clear view on the low-intensity signals.

It is also possible that the initially populated doubly excited state decays radiatively to a state that decays nonradiatively.

Independent-electron models, such as the extended classical overbarrier model [9,10], predict the sequential population of symmetrical ( $n, n'$ ) with  $n = n'$  or quasisymmetrical ( $n, n \approx n'$ ) states. This has been confirmed in many studies [1]. Such states have generally low fluorescence yields and decay predominantly by autoionization. Since the nonradiative transition rate is dependent on the overlap of the electron wave functions, asymmetrical ( $n, n' \gg n$ ) states generally have a larger probability for radiative stabilization than the (quasi)symmetrical ones. Theoretical investigations revealed however, that the stabilization ratio changes from state to state and is particularly sensitive to the main angular momentum quantum number  $J$  [11]. In specific collision systems with projectile ion charges  $6 \leq q \leq 10$  unexpected large fluorescence yields have been found, also for symmetrical and quasisymmetrical states [12,13]. The theoretically calculated stabilization ratios [14],  $P_{\text{rad}} = \sigma_{\text{TDC}} / \sigma_{\text{ADC}} + \sigma_{\text{TDC}}$ , were much lower than the experimentally reported values [12].  $\sigma_i$  denotes the fraction of the projectiles stabilizing through the processes as described above. The discrepancy initiated several studies and extensive discussions [11,15]. Due to the strong term dependence of the nonradiative probability, it is essential to start any discussion on the stabilization ratio with knowledge of which states are populated in the manifold. Such experimental information is very scarce due to the complexity of the doubly excited states. High-resolution measurements are necessary.

By combining Auger data and extreme ultraviolet (EUV) data, we have obtained new information on which states initially are populated and how the decay through the decay

channels takes place. A detailed picture of the decay path of doubly excited states populated in collision systems such as presented here is not only important for an understanding of the collision dynamics of DC processes, but also for charge-exchange-based diagnostic techniques in plasma experiments.

## II. EXPERIMENTAL METHODS

### A. EUV spectroscopy

The presented photon data were recorded at the University of Nevada, Reno Electron Cyclotron Resonance (ECR) multicharged ion facility. The  $^{20}\text{Ne}^{8+}$  ions were mass and charge analyzed with a  $90^\circ$  dipole magnet, and led through a gas cell. During the measurements, the background pressure in the beam line was  $\leq 10^{-8}$  Torr, and the background pressure in the collision chamber, containing the target cell, was  $\leq 2 \times 10^{-6}$  Torr. The length of the beam line was 4.0 m, and the distance crossed by the projectile ions in the collision chamber approaching the gas cell was 25 cm. The effective target cell length was 40 mm. The ion-beam current was measured behind the target cell with an 8.0-cm-deep Faraday cup. Provision was made to suppress secondary electrons. Measured without target gas, the electrical ion-beam current was typically  $0.25 \mu\text{A}$ . The entrance and exit apertures of the target cell were 3.0 and 4.0 mm in diameter, respectively. The attenuation of the electrical ion-beam current was 9%.

Photons in the 60–140-Å wavelength range were recorded at an angle of  $90^\circ$  with respect to the ion-beam axis with a grazing incidence spectrometer [16]. The efficiency of the two-dimensional multichannel plate detector was en-

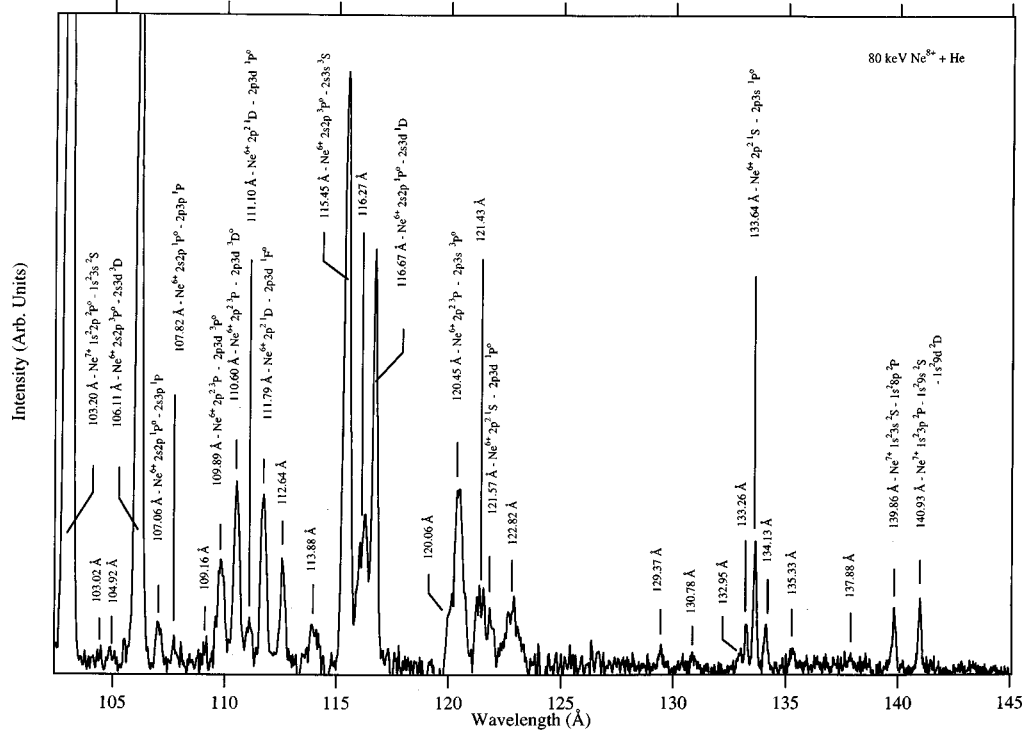


FIG. 2. As in Fig. 1 for the 102.5–145-Å wavelength range.

hanced with a CsI coating and an electron capturing field, provided by a grid in front of the detector. The measured intensities are corrected for the spectral photoefficiency of CsI [17]. The energy-dependent reflectance of the gratings and the polarization of the soft-x-ray radiation has not been taken into account. The uncertainty caused by this approximation is expected to be small compared to other uncertainties. The interaction length viewed by the instrument was 30 mm. The lifetime of the populated doubly excited  $\text{Ne}^{8+}$  states is  $\approx 10^{-11}$  s, and the ions move only some  $\mu\text{m}$  in that time. Therefore the populated states not decaying in the observation region of the instrument can be neglected. The wavelength scale of the photon spectra is fixed using well known SC emission lines [18].

The instrument records spectra with a wavelength span of typically 25 Å, depending on the energy region recorded. The recording of a large energy region, as presented in this paper, takes place by mounting several spectra together. The individual spectra are normalized to each other by utilizing the signals appearing in overlapping wavelength regions. They are recorded as two-dimensional data files, containing the spectroscopic information disturbed by the imaging errors inherent to the use of spherical gratings with grazing incidence in the soft-x-ray wavelength region. The imaging errors are corrected by using a statistical procedure.

For a correct interpretation of the signals due to DC the measurements have to take place under single collision conditions. The probability for the population of a  $\text{Ne}^{6+}1s^2nl'n'l'$  state via two sequential SC processes (double collisions) has to be small relatively to the probability for the population of a  $\text{Ne}^{6+}1s^2nl'n'l'$  state via a two-electron transfer process (DC). This was checked by observing the relative intensities of the signals as a function of the pressure in the gas cell. The pressure in the gas cell is kept low enough to ensure single-collision conditions.

We are aware of the presence of a metastable ( $1s2s^3S$ )  $\text{Ne}^{8+}$  fraction in the projectile ion beam. In this presentation we will only discuss electron-transfer processes to the ground-state  $\text{Ne}^{8+}$  projectile ions. The influence of the metastable fraction will be the subject of a forthcoming paper.

## B. Electron spectroscopy

A beam of  $^{20}\text{Ne}^{8+}$  ions delivered by the Lawrence Berkeley Laboratory ECR ion source with a kinetic energy of 80 keV was mass and charge analyzed and led to the experimental apparatus for zero-degree electron spectroscopy. A detailed description of the setup can be found in Ref. [19]. The

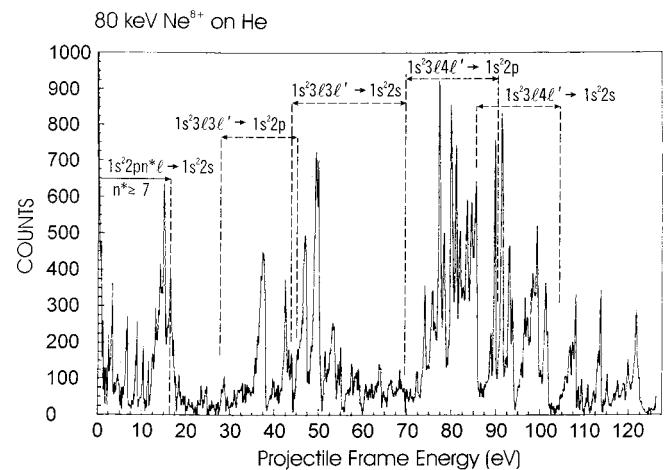


FIG. 3. Typical zero-degree Auger electron spectrum between 0 and 130 eV for the  $\text{Ne}^{8+} + \text{He}$  collision system at  $4.0 \text{ keV amu}^{-1}$ . The electron energies are given in the projectile emitter frame. Identification of the electron signals and a comparison of the experimental and theoretical results are displayed in Tables IV, V, and VII.

TABLE I. Identified SC signals in the EUV data as displayed in Figs. 1 and 2.

Wavelength (Å)	Assignment	Comment
67.32	$\text{Ne}^{7+}1s^22s^2S-1s^24p^2P^o$	
67.84		unassigned
70.40–72.17	unresolved signals	unassigned
73.53	$\text{Ne}^{7+}1s^22p^2P^o-1s^24d^2D$	
74.60	$\text{Ne}^{7+}1s^22p^2P^o-1s^24s^2D$	
88.11	$\text{Ne}^{7+}1s^22s^2S-1s^23p^2P^o$	
98.22	$\text{Ne}^{7+}1s^22p^2P^o-1s^23d^2D$	
103.02	$\text{Ne}^{7+}1s^22p^2P^o-1s^23s^2S$	
132.95		blend sc/dc
133.27		unassigned
134.12	$\text{Ne}^{7+}1s^23s^2S-1s^29p^2P$	
139.80	$\text{Ne}^{7+}1s^23s^2S-1s^28p^2P$	
140.93	$\text{Ne}^{7+}1s^23p^2P-1s^29s,9d^2D$	blend

vacuum in the beam transport system was  $\leq 5 \times 10^{-8}$  Torr. The gas pressure in the target cell was regulated to a pressure of  $3 \times 10^{-5}$  Torr, and controlled by an absolute Baratron gauge. The target cell was 4.0 cm long. Single-collision conditions were assured by observing the relative intensities of the signals as a function of the gas cell pressure.

### III. RESULTS AND DISCUSSION

All results were obtained at 10.0 qkeV ( $q=8$ ) collision energy and are shown in Figs. 1 and 2 (EUV spectrum) and Fig. 3 (zero-degree Auger electron spectrum). All identified EUV transitions are displayed in Tables I (SC) and II (TDC). To distinguish SC and TDC signals in the EUV spectra, we compared with the EUV spectrum from the  $\text{Ne}^{7+}+\text{He}$  collision system that was recorded under identical experimental conditions. Signals in the EUV spectra with  $\text{Ne}^{8+}$  projectiles that are found in the EUV spectra with  $\text{Ne}^{7+}$  projectiles with larger intensity are SC lines. In a wavelength area smaller than 85 Å, the efficiency of the instrument is unexpectedly low. We do not have objective means to correct for this instrumental feature, and exclude this wavelength area from the presented relative intensity calibration. Well-known SC lines are used to wavelength calibrate the EUV spectrum [18].

#### A. Atomic data for doubly excited Be-like neon

In general, little is known about autoionization and radiative decay rates for doubly excited states. To interpret the combined set of electron and photon data, an extensive atomic data set has been calculated. To calculate the level energies  $E$ , wavelengths  $\lambda$ , radiative probabilities  $A_r^{sf}$ , and the sum over all lower levels,  $\sum_f A_r^{sf}$ , we used a computational method comprising three codes: SUPERSTRUCTURE [20], DWMDUB [21] and AUTOLSI [22] have been used. The most important of these is SUPERSTRUCTURE.

##### 1. SUPERSTRUCTURE

This code is appropriate for the calculation of large quantities of atomic data as it uses a model potential, which is of

TABLE II. Identified TDC signals in the EUV data as displayed in Figs. 1 and 2.

Wavelength (Å)	Assignment	Comment
70.40–72.17		unresolved lines
75.73	$\text{Ne}^{6+}2s^2^1S-2s4p^1P^o$ blend $2s2p^3P^o-2s5s^3S$	
82.17	$\text{Ne}^{6+}2s2p^3P^o-2s4d^3D$	
82.96	$\text{Ne}^{6+}2s^2^1S-2p3d^1P^o$	
84.23	$\text{Ne}^{6+}2s2p^3P^o-2s4s^3S$	
89.40	$\text{Ne}^{6+}2s2p^1P^o-2s4d^1D$	
91.61	$\text{Ne}^{6+}2s2p^1P^o-2s4s^1S$	
94.39	$\text{Ne}^{6+}2s2p^3P^o-2p3p^3P$	
94.99	$\text{Ne}^{6+}2s2p^3P^o-2p3p^3S$	
95.86	$\text{Ne}^{6+}2s2p^3P^o-2p3p^3D$	
97.20	$\text{Ne}^{6+}2p^2^3P-2s4p^3P^o$	
97.46	$\text{Ne}^{6+}2s^2^1S-2s3p^1P^o$	
99.14		unassigned
99.72	$\text{Ne}^{6+}2p^2^1D-2s4p^1P^o$ $\text{Ne}^{6+}2s2p^1P^o-2p3p^1S$	
100.20		unassigned
100.94		unassigned
102.10	$\text{Ne}^{6+}2s2p^1P^o-2p3p^1D$	
104.46		unassigned
106.10	$\text{Ne}^{6+}2s2p^3P^o-2s3d^3D$	
107.07	$\text{Ne}^{6+}2s2p^1P^o-2p3p^1P$	
107.80		unassigned
109.90	$\text{Ne}^{6+}2p^2^3P-2p3d^3P^o$	
110.61	$\text{Ne}^{6+}2p^2^3P-2p3d^3D^o$	
111.17	$\text{Ne}^{6+}2p^2^1D-2p3d^1P^o$	
111.82	$\text{Ne}^{6+}2p^2^1D-2p3d^1F^o$	
112.67	$\text{Ne}^{6+}2p^2^3P-2p3d^3F^o$	
115.45	$\text{Ne}^{6+}2s2p^3P^o-2s3s^3S$	
116.17	$\text{Ne}^{6+}2p^2^1D-2p3d^3F^o$	
116.67	$\text{Ne}^{6+}2s2p^1P^o-2s3d^1D$	
119.60		unassigned
120.04		unassigned
120.45	$\text{Ne}^{6+}2p^2^3P-2p3s^3P^o$	blend
121.54	$\text{Ne}^{6+}2p^2^1S-2p3d^1P^o$	
122.31	$\text{Ne}^{6+}2p^2^1D-2p3s^1P^o$	
123.36		unassigned
123.81	$\text{Ne}^{6+}2s^2^1S^o-2p3s^1P^o$	
124.76		unassigned
129.37	$\text{Ne}^{6+}2s2p^1P^o-2s3s^1S$	
130.90		unassigned
133.64	$\text{Ne}^{6+}2p^2^1S-2p3s^1P^o$	
135.31	$\text{Ne}^{6+}2p^2^3P-2s3p^3P^o$	
137.88		unassigned
140.93	$\text{Ne}^{6+}2p^2^3P-2s3p^1P^o$	blend

the Thomas-Fermi-Dirac Amaldi type. The method takes into account the average effect of repulsion of other electrons which leads to a central potential  $V(r)$ , satisfying the following boundary conditions

$$\begin{aligned}
 V(r) &= Z/r \quad \text{when } r \rightarrow 0 \\
 &= (Z-N+1)/r \quad \text{when } r \rightarrow \infty,
 \end{aligned}$$

where  $Z$  is the nuclear charge and  $N$  the number of electrons ( $z = Z - N$ ).

To obtain greater flexibility, a scaling parameter  $\lambda_l$  is introduced such that all the radial functions with the same  $l$  are calculated in the same potential and are therefore orthogonal to each other, giving

$$V(r) = V(\lambda_l, r).$$

This scaling parameter  $\lambda_l$  can be obtained by minimizing preselected terms.

The program uses multiconfigurational wave functions to derive level energies and wavelengths. For the calculation of the atomic data for highly charged atoms, it is necessary to take relativistic corrections into account. The semirelativistic Breit-Pauli Hamiltonian in which the relativistic corrections are treated as perturbations is convenient. This Hamiltonian is given by the expression

$$H = H^{\text{BP}} = H^{\text{NR}} + V^R,$$

where  $H^{\text{NR}}$  is the nonrelativistic Hamiltonian, and  $V^R$  corresponds to the one- operators (mass, Darwin, spin-orbit) and two-body operators (contact spin-spin, Darwin, orbit-orbit, spin-other-orbit, mutual spin-orbit, and spin-spin) of the relativistic corrections.

The development of the wave function of a level  $\Delta J$  on the multiconfigurational basis in the intermediate coupling  $tJ$ , called *level*, is obtained by the diagonalization of the total Hamiltonian  $H^{\text{BP}}$ . This is expressed as

$$\psi(\Delta J, M) = \sum_t C(tJ, \Delta J) \Phi'(tM_L M_S),$$

where  $\Phi$  is obtained from the  $LS$  coupling wave function of the term  $t = C\beta SL$  by

$$\Phi(tJ, M) = \sum_{M_L M_S} C_{M_L M_S M_J}^{LSJ} \Phi'(tM_L M_S),$$

where  $\beta$  is a degeneracy parameter taking into account those cases where a configuration  $C$  gives rise to more than one term with the same  $\mathbf{LS}$ . The coefficients  $C(t\mathbf{J}, \Delta\mathbf{J})$  are the *level* mixing coefficients.  $C_{M_L M_S M_J}^{LSJ}$  are Clebsch-Gordan coefficients, and  $M_L$ ,  $M_S$  and  $M_J$  are the projections of the momenta  $\mathbf{L}$ ,  $\mathbf{S}$ , and  $\mathbf{J}$ , respectively.

For highly ionized elements, autoionization processes are weak enough to be treated by perturbation theory. The autoionization probability  $A_a^{\text{Si}}$  is given by

$$A_a^{\text{Si}} = \frac{2\pi}{\hbar} |\langle \Psi_F^i(E_S) | H - E_S | \Psi_S \rangle|^2$$

where

$$E_S = \langle \Psi_S | H | \Psi_S \rangle$$

and  $\Psi_S$  and  $\Psi_F^i$  are the initial *bound* and final *free* states, respectively. The energy  $E_S$  of the free state  $\Psi_F^i$  is taken the same as that of the bound state  $\Psi_S$ . The wave functions  $\Psi_F^i$  are normalized to the Dirac functions:

$$\langle \Psi_F^i(E) | \Psi_F^i(E') \rangle = \delta(E - E') \delta_{ii'}.$$

The free wave function  $\Psi_F^i$  corresponds to an autoionizing channel, i.e., a level  $\Delta J_i$  for the autoionizing ion plus the free electron ( $\epsilon, l$ ), where  $\epsilon$  and  $l$  are the energy and angular momentum of the free electron. As long as only large autoionization probabilities are required, the relativistic behavior of the free electron can be ignored; then the operators  $\mathbf{K}$  and  $\mathbf{J}$  commute with the Hamiltonian:

$$\mathbf{J}_i = \mathbf{L}_i + \mathbf{S}_i,$$

$$\mathbf{K} = \mathbf{J}_i + l,$$

$$\mathbf{J} = \mathbf{K} + s,$$

where  $s$  is the free electron spin ( $s = 1/2$ ).

$$A_a^{\text{Si}} = \frac{2\pi}{\hbar} \sum_{lk} \left| \sum_{t_i} C(\Delta J_i, t_i J_i) X(SLJ, S_i L_i J_i, lK) \right. \\ \left. \times \langle t_i l J | H - E_S | t J \rangle C(tJ, \Delta J) \right|^2,$$

where  $t_i = C_i \beta_i S_i L_i$  is a term for the  $(z+1)$  ion and,  $X(SLJ, S_i L_i J_i, lK)$  can be expressed [23] as a function of the Racah recoupling coefficient  $W$ :

$$X(SLJ, S_i L_i J_i, lK) = W(L_i S_i J_i, L_i K) W(L J S_i \frac{1}{2}, SK) \\ \times [(2S+1)(2L+1)(2K+1) \\ \times (2J_i+1)]^{1/2}.$$

In the present work we have  $V^r$  only in the one-body operators. The calculations yield the energies  $A_a$ ,  $A_{ij}$ , and  $\omega_T$  (the total fluorescence yield). From these values, the Auger electron energies for stabilization toward different continua are deduced.

In the first step, the code determined a set of nonrelativistic wave functions by diagonalization of the nonrelativistic Hamiltonian on a set of chosen configurations. The single-electron wave functions are calculated in a so called Thomas-Fermi-Dirac-Amaldi potential for each angular momentum  $l$ . The scaling parameters have been iterated to give the minimum energy of a term or a group of terms. In the present work the parameters are obtained by the minimization procedure of the energy sum of all terms belong to the following configurations:  $1s^2 2s^2$ ,  $1s^2 2s 2p$  for  $\lambda_s$  and  $1s^2 2s^2$ ,  $1s^2 2s 2p$ ,  $1s^2 2p^2$ ,  $1s 2s 2p^2$ , and  $1s 2p^3$  for  $\lambda_p$ . The values obtained are 1.320 for  $\lambda_s$  and 1.578 for  $\lambda_p$ . We put  $\lambda_p = \lambda_a = \lambda_f$ . In a second step the program uses these scaling parameters in a multiconfigurational basis to calculate the nonrelativistic and relativistic level energies diagonalizing the matrices corresponding to the nonrelativistic and relativistic Hamiltonians, respectively. Finally the wavelengths and radiative probabilities are calculated. The multiconfigurational basis set used in the present work contains all the configurations  $1s^2 n l n' l'$ , with  $(n = n' = n, l = 0, 1) + (n = n' = 3, l = 0, 1, 2) + (n = 3n' = 4, l = 0, 1, 2, 3) + (n = n' = 4, l = 0, 1, 2, 3)$ , which corresponds to 29 configurations, 114 terms, and 311 levels.

TABLE III. Calculated wavelengths and transition probabilities of transitions from  $\text{Ne}^{6+}(1s^22l3l')$ .

Transition	Wavelength (Å)	$A_r(s^{-1})$	$\Sigma A_r(s^{-1})$
$1s^22p3d^1D_2-1s^22s2p^3P_1$	93.9650	1.202+10	
$1s^22p3d^1D_2-1s^22s2p^3P_2$	94.0551	3.851+10	5.181+10
$1s^22p3p^3P_2-1s^22s2p^3P_0$	93.9734	1.526+10	
$1s^22p3p^3P_2-1s^22s2p^3P_1$	94.0179	1.128+10	
$1s^22p3p^3P_2-1s^22s2p^3P_2$	94.1081	2.409+10	5.186+10
$1s^22p3p^3P_0-1s^22s2p^3P_1$	94.0498	5.063+10	5.184+10
$1s^22p3p^3S_1-1s^22s2p^3P_1$	94.7063	2.115+10	
$1s^22p3p^3S_1-1s^22s2p^3P_2$	94.7978	2.955+10	5.952+10
$1s^22p3p^3D_2-1s^22s2p^3P_2$	95.6996	2.277+10	3.046+10
$1s^22p3p^3D_3-1s^22s2p^3P_2$	95.7060	2.979+10	3.026+10
$1s^22s3p^1P_0-1s^22s^2S_0$	97.3801	1.069+11	
$1s^22s3p^3P_0-1s^22p^2D_2$	126.3240	1.214+10	1.195+11
$1s^22p3p^1S_0-1s^22s2p^1P_1$	100.2078	2.979+10	3.026+10
$1s^22p3p^1D_2-1s^22s2p^3P_1$	103.2836	2.943+10	3.152+10
$1s^22s3d^3D_1-1s^22s2p^3P_0$	105.8749	1.2784+11	
$1s^22s3d^3D_1-1s^22s2p^3P_1$	105.9313	9.578+10	2.300+11
$1s^22s3d^3D_2-1s^22s2p^3P_1$	105.9258	1.724+11	
$1s^22s3d^3D_2-1s^22s2p^3P_2$	106.0399	5.740+10	2.298+11
$1s^22s3d^3D_3-1s^22s2p^3P_2$	106.0308	2.295+11	2.295+11
$1s^22p3d^3P_2-1s^22p^2P_1$	109.8022	2.433+10	
$1s^22p3d^3P_2-1s^22p^2P_2$	109.9221	1.333+11	1.549+11
$1s^22p3d^3P_1-1s^22p^2P_0$	109.6943	4.144+10	
$1s^22p3d^3P_1-1s^22p^2P_1$	109.7569	4.818+10	
$1s^22p3d^3P_1-1s^22p^2P_2$	109.8767	6.806+10	1.592+11
$1s^22p3d^3D_1-1s^22p^2P_0$	110.5208	1.731+11	
$1s^22p3d^3D_1-1s^22p^2P_1$	110.5844	1.128+11	2.926+11
$1s^22p3d^3D_2-1s^22p^2P_1$	110.5593	2.335+11	
$1s^22p3d^3D_2-1s^22p^2P_2$	110.6808	5.716+10	2.918+11
$1s^22p3d^1P_1-1s^22p^2D_2$	111.0315	1.456+10	
$1s^22p3d^1P_1-1s^22p^2S_0$	121.8942	2.019+11	2.259+11
$1s^22p3d^1F_3-1s^22p^2D_2$	111.4534	3.632+11	2.928+11
$1s^22s3s^3S_1-1s^22s2p^3P_0$	115.4160	5.687 +09	
$1s^22s3s^3S_1-1s^22s2p^3P_1$	115.4831	1.710 +10	
$1s^22s3s^3S_1-1s^22s2p^3P_2$	115.6192	2.866 +10	5.145+10
$1s^22p3d^3F_2-1s^22p^2D_2$	116.7345	4.996+10	5.060+10
$1s^22p3d^1D_2-1s^22p^2D_2$	116.8710	5.162+10	5.214+10
$1s^22s3d^1D_2-1s^22s2p^1P_1$	117.2764	1.556+11	1.556+11
$1s^22s3s^3P_2-1s^22s2p^3P_1$	120.2116	1.017 +10	
$1s^22s3s^3P_2-1s^22s2p^3P_2$	120.3562	3.034 +10	4.130+10
$1s^22s3s^1S_1-1s^22p^2P_1$	120.4263	4.025+10	4.100+10
$1s^22p3s^3P_1-1s^22p^2P_0$	120.2823	1.345+10	
$1s^22p3s^3P_1-1s^22p^2P_1$	120.3576	1.002+10	
$1s^22p3s^3P_1-1s^22p^2P_2$	120.5016	1.686+10	4.110+10
$1s^22s3s^1S_1-1s^22s2p^1P_1$	128.9181	2.145+10	2.145+10

## 2. DWMDUB

This code corresponds to the DISTWAV code [24] modified by Dubau. It determines, in a distorted-wave approximation, the transition matrix elements between the bound and free states.

## 3. AUTOLSI

This code transforms the *LS*-coupling reactance matrix obtained by DWMDUB to an intermediate-coupling one with

the help of term coupling coefficients provided by SUPERSTRUCTURE, and afterwards calculates Auger rates and fluorescence yields. The Auger rates for  $1s^23l3l'$  and  $1s^24l4l'$  are calculated for seven energies of the incident electron equal to 4.0, 6.0, 7.0, 7.5, 7.57, 8.0, and 11 Ry, and between 7.5 and 11 Ry for  $1s^24l4l'$ .

## 4. Theoretical results

In Table III the wavelengths and radiative transition prob-

TABLE IV. Calculated and experimental  $\text{Ne}^{6+}(1s^23l3l')$  singlet and triplet states. For each state we present the energy relative to the ground state  $E$ , the total nonradiative decay probability  $\Sigma A_a$ , the total radiative decay probability  $\Sigma A_r$ , the total fluorescence yield  $\omega_T = \Sigma A_r / (\Sigma A_r + \Sigma A_a)$ , the calculated Auger branching ratio to the  $2s$  continuum BR  $1s^22s$ , and the estimated experimental Auger branching ratio to the  $2s$  continuum BR  $1s^22s$ .  $E_{\text{PCI}}$  gives the approximate calculated energy positions to the  $2s$  ( $2p$ ) continua after correction for the postcollision effect at an observation angle of  $0^\circ$ .  $E_{\text{expt}}$  gives the observed energy positions to the  $2s$  and  $2p$  continua. Some of the signals are assigned to several terms. This means that a unique assignment of the signal is impossible since the experimental resolution is not sufficient. The resolution of the presented data is 0.1 eV.

State	$E$ (eV)	$\Sigma A_a (s^{-1})$	$\Sigma A_r (s^{-1})$	$\omega_T$	BR $1s^22s$	BR <sub>expt</sub> $1s^22s$	$E_{\text{PCI}}$ (eV)	$E_{\text{expt}}$ (eV)
$3s^2\ ^1S$	253.68	9.55+13	1.02+11	1.07-03	0.98	0.87	46.3/30.4	46.1/30.5
$3s3p\ ^3P$	256.41	9.04+13	1.06+11	1.17-03	0.99		49.1/33.1	-/33.1
$3s3d\ ^1D$	259.93	3.02+14	3.66+10	1.21-04	0.35	0.39	52.6/36.5	53.1/37.0
$3s3p\ ^1P$	260.12	5.26+14	1.02+11	1.07-03	0.35	0.39	52.6/36.5	53.1/37.0
$3s3d\ ^3D$	261.32	2.60+13	2.55+11	9.71-03	0.55	0.23	54.0/38.0	54.3/37.9
$3p^2\ ^3P$	262.19	1.72+14	1.56+11	9.06-04	0	0.77	54.9/38.9	54.8/39.1
$3p3d\ ^3F$	264.20	2.54+12	2.82+11	9.99-02	0.30	0.48	56.9/40.9	57.0/40.9
$3p3d\ ^1D$	264.35		3.51+10			0.45	57.1/41.1	57.0/40.9
$3p^2\ ^1S$	265.24	1.05+15	3.51+11	3.34-04	0.12		58.0/42.0	58.1/-
$3p^2\ ^1D$	265.71	3.84+14	5.50+10	1.43-04	0.29	0.23	58.4/42.4	58.4/42.4
$3p3d\ ^3D$	266.50	1.15+14	2.90+11	2.52-03	0		59.2/43.2	59.3/43.1
$3p3d\ ^3P$	267.02	4.84+13	2.85+11	5.85-03	0.09		59.7/43.7	-/43.7
$3d^2\ ^3F$	268.56	1.76+14	4.44+11	2.52-03	0	0.26	61.3/45.3	61.4/45.4
$3p3d\ ^1F$	270.11	3.26+14	2.91+10	8.93-05	0	0.13	62.8/46.8	62.9/47.0
$3d^2\ ^1G$	270.66	1.04+15	4.33+10	4.16-05	0.17	0.53	63.4/47.4	63.6/47.6
$3d^2\ ^3P$	271.21	1.38+13	4.38+11	3.08-02	0		63.9/47.9	-/-
$3d^2\ ^1D$	272.56	2.42+14	3.21+10	1.33-04	0.03	0.05	65.3/49.3	65.2/49.5
$3p3d\ ^1P$	272.93	2.16+14	3.17+10	1.47-04	0.02	0.09	65.7/49.7	65.7/50.0
$3d^2\ ^1S$	279.08	1.89+13	3.02+10	1.60-03	0.58	0.75	71.8/55.8	71.7/55.6

abilities of the calculated  $\text{Ne}^{6+}1s^22l3l'$  levels are displayed. In Tables IV, V, and VI, we present the calculated atomic data set as discussed above for doubly excited (3,3), (3,4), and (4,4) states of  $\text{Ne}^{6+}$ .

For each calculated state we present the following data: The energy with respect to the ground state, the total nonradiative transition probability  $\Sigma A_a$ , the total radiative transition probability  $\Sigma A_{ij}$ , the fluorescence yield  $\omega_T$  defined as  $\omega_T = \Sigma A_{ij} / (\Sigma A_{ij} + \Sigma A_a)$ , the branching ratio (BR) to the  $1s^22s$  continuum, the corrected (see below) energy of the electrons in the emitter frame at zero degree observation to the  $2s/2p$  continuum, and the experimentally observed energy of the electrons in the emitter frame to the  $2s/2p$  continua. In Tables V and VI the center of gravity energy of the multiplet is also presented ( $E^{\text{cog}} = [\Sigma_j (2j+1) E_j] / (\Sigma_j 2j + 1)$ ), used to compare with the positions of the signals in the Auger spectra. The theoretical electron energies are corrected by a factor  $\Delta_{\text{BB}} \xi(0^\circ)$ , where  $\Delta_{\text{BB}}$  is the energy shift due to the post-collision interaction (PCI) as described by Barker and Berry [25], and the factor  $\xi(0^\circ)$  takes into account the dependence of the PCI effect on the angle of emission of the electron [26].

### B. Single-electron transfer

The most intense lines are Li-like SC channels corresponding to radiative decay from  $\text{Ne}^{7+}(1s^2nl)$  initial states. We observe decay from  $n$  up to 9. The SC processes popu-

late dominantly  $n=4$ . This is known from energy gain measurements [27]. The intensity of the  $n=4$  signals in our EUV spectrum is too low compared to the intensity of the  $n=3$  signals, since it is known from previous measurements [4–6] that SC mostly populates  $n=4$  levels. This is also predicted by the classical overbarrier model [9,10]. The discrepancy is due to the low reflectivity of the grating in the wavelength region 60–80 Å. A comparison of the relative intensities in the present EUV spectra and spectra measured by Politus *et al.* [6] show an exponential decrease of the sensitivity of our instrument in the wavelength range smaller than 85 Å.

The  $n=3$  levels are partly populated via cascades. The identifications of the SC EUV signals, as presented in Table I, are based on known transitions [18] and the results of new calculations, displayed in Table III. Excluding the low-wavelength region, we observe that the relative intensities of the SC lines are identical to previous studies [4–6]. The unassigned signals in Tables I and II could be due to the stabilization after electron capture to the metastable  $\text{Ne}^{8+}(1s2s^3S)$  fraction in the beam. This will not be discussed in the present paper.

In the wavelength region above 100 Å, the efficiency of the grazing incidence instrument is relatively high. We observe the  $1s^29p\ ^2P-1s^23s\ ^2S$  transition at 134.13 Å, the  $1s^28p\ ^2P-1s^23s\ ^2P$  at 139.86 Å and the  $1s^29s\ ^2P/1s^29d\ ^2P-1s^23p\ ^2P$  transition at 140.93 Å. These observations are not in disagreement with the extended classical overbarrier model [9,10], since the probability distribution to populate

TABLE V. As in Table IV for  $\text{Ne}^{6+}(1s^23l4l')$  singlet and triplet states.  $E_{\text{c.m.}}$  is the center of gravity energy of the multiplet.

State	$E$ (eV)	$E_{\text{c.m.}}$	$\Sigma A_a(s^{-1})$	$\Sigma A_r(s^{-1})$	$\omega_T$	BR $1s^22s$	$E_{\text{PCI}}$ (eV)	$E_{\text{expt}}$ (eV)
$3s4s^3S_1$	295.29		6.89+11	1.25+10	1.80-02	1.0	88.0/72,0	87.9/72.2
$3s4s^1S_0$	296.10		5.98+13	5.60+09	9.36-05	1.0	89.0/72,8	88.9/-
$3s4p^1P_1$	297.09		3.55+13	1.53+10	4.30-04	0.53	89.8/73.8	90.0/73.9
$3s4p^3P_0$	297.45		5.06+13	1.26+09	2.48-05	0.55	90.2/74.2	-/-
$3s4p^3P_1$	297.46	297.46	5.06+13	1.26+09	2.50-05	0.55	90.2/74.2	-/-
$3s4p^3P_2$	297.47		5.06+13	1.26+09	2.50-05	0.55	90.2/74.2	-/-
$3s4d^3D_1$	298.78		1.00+13	2.54+10	2.53-03	0.67	91.5/75.5	-/75.6
$3s4d^3D_2$	298.79	298.80	1.00+13	2.54+10	2.53-03	0.67	91.5/75.5	-/75.6
$3s4d^3D_3$	298.81		1.00+13	2.54+10	2.52-03	0.67	91.5/75.5	-/75.6
$3s4d^1D_2$	298.98		7.89+13	1.14+10	1.44-04	0.68	91.7/75.7	91.7/75.8
$3s4f^3F_2$	300.24		2.83+12	3.81+10	1.33-02	0.82	93.0/77.0	93.1/-
$3s4f^3F_3$	300.25	300.25	3.00+13	3.81+10	1.26-02	0.87	93.0/77.0	93.1/-
$3s4f^3F_4$	300.25		3.00+12	3.82+10	1.25-02	0.87	93.0/77.0	93.1/-
$3p4s^3P_0$	300.79		1.30+13	1.04+10	7.79-04	0.42	93.5/77.5	-/-
$3p4s^3P_1$	300.81	300.83	1.32+13	1.04+10	7.85-04	0.42	93.5/77.5	-/-
$3p4s^3P_2$	300.86		1.32+13	1.05+10	7.94-04	0.42	93.5/77.5	-/-
$3s4f^1F_3$	300.95		5.93+13	4.24+10	7.15-04	0.02	93.7/77.6	93.7/77.4
$3p4p^1P_1$	301.30			1.04+10			94.0/78.0	-/-
$3p4s^1P_1$	301.69		2.03+14	8.64+09	4.26-05	0.32	94.4/78.3	-/78.4
$3p4p^3D_1$	302.21		4.86+12	4.56+09	9.37-04	0.20	95.0/79.0	-/79.0
$3p4p^3D_2$	302.23	302.25	5.12+12	4.61+09	8.99-04	0.19	95.0/79.0	-/79.0
$3p4p^3D_3$	302.27		4.04+12	4.69+09	1.16-03	0.24	95.0/79.0	-/79.0
$3p4p^3S_1$	302.34		2.58+13	1.12+10	4.36-04	0.14	95.1/79.0	-/79.0
$3p4p^3P_0$	302.34			6.50+09			95.1/79.1	-/79.0
$3p4p^3P_1$	302.38	302.39		7.40+09			95.1/79.1	-/79.0
$3p4p^3P_2$	302.41			6.48+09			95.1/79.1	-/79.0
$3p4d^1D_2$	303.27			1.19+10			96.0/80.0	-/79.9
$3p4p^3D_1$	303.46		4.86+12	4.56+09	9.38-04	0.20	96.2/80.2	-/79.9
$3p4p^3D_2$	303.48	303.48	5.12+12	4.61+09	8.98-04	0.19	96.2/80.2	-/79.9
$3p4p^3D_3$	303.50		4.36+12	4.69+09	1.97-03	0.22	96.2/80.2	-/79.9
$3p4p^1D_2$	303.72		2.22+14	1.71+10	7.70-05	0.60	96.4/80.4	-/-
$3p4d^3F_2$	304.03		1.93+12	4.80+09	2.49-03	0.43	96.8/80.8	-/-
$3p4d^3F_3$	304.05	304.06	2.01+12	4.82+09	2.39-03	0.42	96.8/80.8	-/-
$3p4d^3F_4$	304.08		1.88+12	4.72+09	2.53-03	0.44	96.8/80.8	-/-
$3p4f^1F_3$	304.06		1.44+11	5.03+10	2.58-01	0.74	96.8/80.8	-/-
$3p4f^3G_3$	304.20		2.20+12	6.12+10	2.70-02	0.12	96.9/80.9	97.1/81.2
$3p4f^3G_4$	304.22	304.23	2.22+12	6.14+10	2.69-02	0.12	96.9/80.9	97.1/81.2
$3p4f^3G_5$	304.25		2.15+12	6.17+10	2.79-02	0.12	96.9/80.9	97.1/81.2
$3p4p^1S_0$	304.36		5.29+14	1.25+10	2.36-05	0.11	97.0/80.7	97.1/81.2
$3p4f^3F_2$	304.43			2.73+10			97.2/81.2	97.1/81.2
$3p4f^3F_3$	304.44	304.44		2.75+10			97.2/81.2	97.1/81.2
$3p4f^3F_4$	304.45			2.75+10			97.2/81.2	97.1/81.2
$3p4d^3P_2$	304.68		2.35+13	1.52+10	6.47-04	0.04	97.4/81.4	-/81.2
$3p4d^3P_1$	304.69	304.68	2.35+13	1.53+10	6.50-04	0.04	97.4/81.4	-/81.2
$3p4d^3P_0$	304.70			1.53+10				
$3p4d^1F_3$	304.87		1.22+11	3.81+10	3.13-01	0.09	97.6/81.5	-/81.2
$3d4d^3D_3$	305.41			3.70+10			98.1/82.1	98.2/82.0
$3d4d^3D_2$	305.41	305.41		3.67+10			98.1/82.1	98.2/82.0
$3d4d^3D_1$	305.41			3.65+10			98.1/82.1	98.2/82.0
$3d4d^1F_3$	305.35			1.26+10			98.1/82.1	98.2/82.0
$3p4f^1G_4$	305.85		3.10+14	2.57+09	8.29-06	0.27	98.5/82.4	-/82.5
$3p4d^1P_1$	305.94		8.53+11	2.99+10	3.39-02	0.97	98.7/82.7	-/82.6
$3d4f^1G_4$	306.08			1.32+10			98.8/82.8	-/-
$3d4d^1P_1$	306.15			2.14+10			98.9/82.9	-/-

TABLE V. (Continued).

$3d4d^3G_3$	306.14		1.68+13	8.14+08	4.84-05	1.0	98.9/82.9	-/-
$3d4d^3G_4$	306.16	306.16	1.69+13	7.56+08	4.47-05	1.0	98.9/82.9	-/-
$3d4d^3G_5$	306.17		1.70+13	6.87+08	4.02-05	1.0	98.9/82.9	-/-
$3d4f^3H_4$	306.17	306.17	1.09+13	3.90+07	3.57-06	1.0	98.9/82.9	-/-
$3d4f^3H_5$	306.18		1.09+13	3.66+05	3.29-08	1.0	98.9/82.9	-/-
$3d4d^3F_2$	306.58			3.34+10			99.3/83.3	-83.6
$3d4d^3F_3$	306.59	306.59		3.33+10			99.3/83.3	-83.6
$3d4d^3F_4$	306.60			3.35+10			99.3/83.3	-83.6
$3p4f^3D_3$	306.65		1.37+12	2.45+10	1.76-02	0.98	99.4/83.4	99.4/83.6
$3p4f^3D_2$	306.65	306.65	1.49+12	2.48+10	6.63-02	0.98	99.4/83.4	99.4/83.6
$3p4f^3D_1$	306.66		1.42+12	2.49+10	1.73-02	0.98	99.4/83.4	99.4/83.6
$3p4f^1D_2$	306.89		1.10+13	2.42+10	2.20-03	1.0	99.6/83.6	99.4/83.6
$3d4f^3F_4$	306.92		1.47+12	1.88+10	1.27-06	1.0	99.6/83.6	99.4/83.6
$3d4f^1D_2$	307.43			3.38+10			100.2/86.5	100.0/-
$3d4d^3P_0$	307.69			1.72+10			100.4/84.4	-84.6
$3d4d^3P_1$	307.70	307.70		1.72+10			100.4/84.4	-84.6
$3d4d^3P_2$	307.70			1.72+10			100.4/84.4	-84.6
$3d4d^3S_1$	307.76		1.48+12	1.88+10	1.25-02	0.99	100.5/84.5	-/-
$3d4d^1D_2$	308.71		6.07+13	3.13+10	5.15-04	0.04	101.4/85.4	101.2/85.6
$3d4d^1G_4$	308.76		2.04+14	5.06+10	2.48-04	0.05	101.5/85.3	-85.6
$3d4f^1F_3$	309.78		2.50+13	5.44+10	2.17-03	0.56	102.5/86.5	102.7/86.7
$3d4f^1H_5$	310.50		1.29+14	7.94+10	6.15-04	0.22	103.2/87.2	-87.2
$3d4f^1P_1$	311.32			4.35+10			104.0/88.0	-87.9
$3d4d^1S_0$	314.41		3.69+12	1.21+10	3.26-02	0.96	107.1/91.1	107.2/-

levels different from the most probable capture levels is described by a Gaussian function in this model, increasing in width with the projectile velocity. Using known cross sections [5] we derived the absolute cross sections for single-electron capture to transitions from  $n=9$  to be  $9.8 \times 10^{-19} \text{ cm}^2$ . Within the obtained accuracy we observe the cross sections for these high- $n$  levels to be identical to each other. We used the Cowan programs [28] to calculate the branching ratios necessary to derive the cross sections. The error in this cross section is 40%. The capture cross section for the most probable capture levels ( $n=4$ ) has been measured by Bonnet *et al.* [5] to be  $7.8 \times 10^{-16} \text{ cm}^2$  ( $\pm 40\%$ ).

From the electron data it is observed that the major part of the DC population is to  $\text{Ne}^{6+}$  (3,3) and (3,4) states. The Auger decay from these states can only decay to the  $2s$  and  $2p$  continua. A very small part of the DC populates  $\text{Ne}^{6+}$  (4,4) states. These can decay to the  $3l$  continua so that the observed  $\text{Ne}^{7+}$  ( $1s^23l$ ) radiation is not entirely originating from SC processes. We will neglect this since the cross section to  $\text{Ne}^{6+}$  ( $n, n'$ ) with  $n$  and  $n' \leq 4$  is certainly much smaller than the SC cross section.

### C. Double-electron transfer

A typical Auger electron spectrum, recorded under the same experimental conditions as the EUV spectrum, is displayed in Fig. 3. An energy diagram is shown in Fig. 4 with the decay path for radiative and nonradiative decay after double-electron transfer (DC). Two-electron transfer processes in this collision system populate mostly (3,3) and (3,4) states. In the low-energy region it is possible to observe the decay from  $2pnl$  ( $n > 6$ ) states. This is shown in Fig. 7. It

is not possible to do a direct comparison between the experimental data and the calculated states since the resolution is insufficient to resolve individual states. However, the center of gravity of the calculated multiplet can be compared with the experimental signals.

#### 1. Radiative decay

Using the atomic structure calculations we identified most of the DC photon signals (Table II). Many transitions from  $\text{Ne}^{6+}$  ( $2l3l'$ ) levels could be identified from tabulated values [18]. The structure of the lowest (2,3) energy levels in  $\text{Ne}^{6+}$  is shown in Figs. 5 and 6 for the singlet and triplet systems,

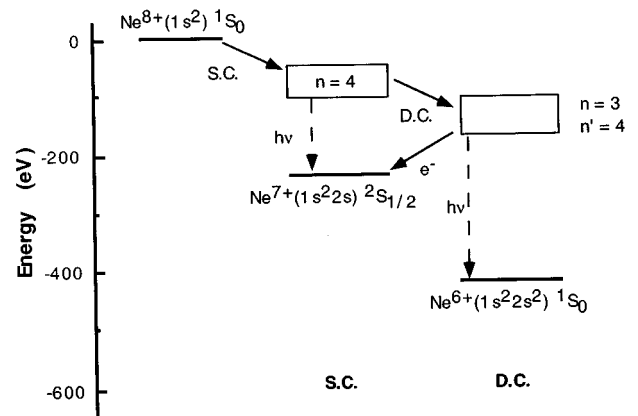


FIG. 4. Schematic energy diagram showing the decay path after single capture (SC) and double capture (DC).

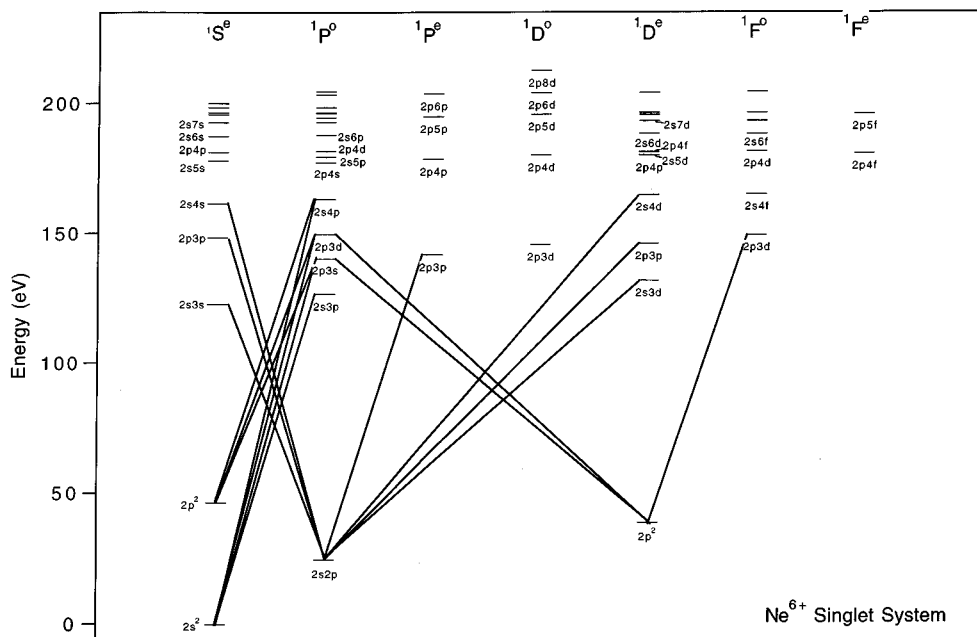


FIG. 5. Grotarian diagram of the lowest (2,3) singlet levels in  $\text{Ne}^{6+}$ . The observed signals are indicated.

respectively. The observed signals are indicated in the diagrams. Only the lowest (2,3) levels are observed in the EUV spectrum. Many triplet signals are observed.

Energy gain measurements [27] recorded at 13.6 keV show that mainly (3,4) and (3,3) states are populated in the ratio 7:3. At 80 keV some population of the (4,4) and (4,5) states is expected. This is observed in the Auger spectrum. Radiative transitions from (3,3) and (3,4) states are difficult to identify due to the complexity of these states. Direct radiative decay from these states is expected to be very weak apart from some states. It has, however, been measured [13]

in comparable collision systems that a non-negligible part of the ions produced after the capture of two electrons decays by stabilizing both electrons. By identifying the decay of  $\text{Ne}^{6+}(2I3I')$  states in the final step of the decay in the EUV spectrum, information on the radiative decay processes populating the (2,3) states is obtained. The Cowan programs are used to calculate which states most probably populate the observed (2,3) states. The most intense even (2,3) states are  $2s3d\ ^3D$ ,  $2s3s\ ^3S$  and  $2s3d\ ^1D$ . These states are mainly populated from the  $3p3d\ ^1,3D$  and  $^3F$  states. The  $2s3s\ ^3S$  term is mainly populated by  $3s4p\ ^1,3P$  states. It is not pos-

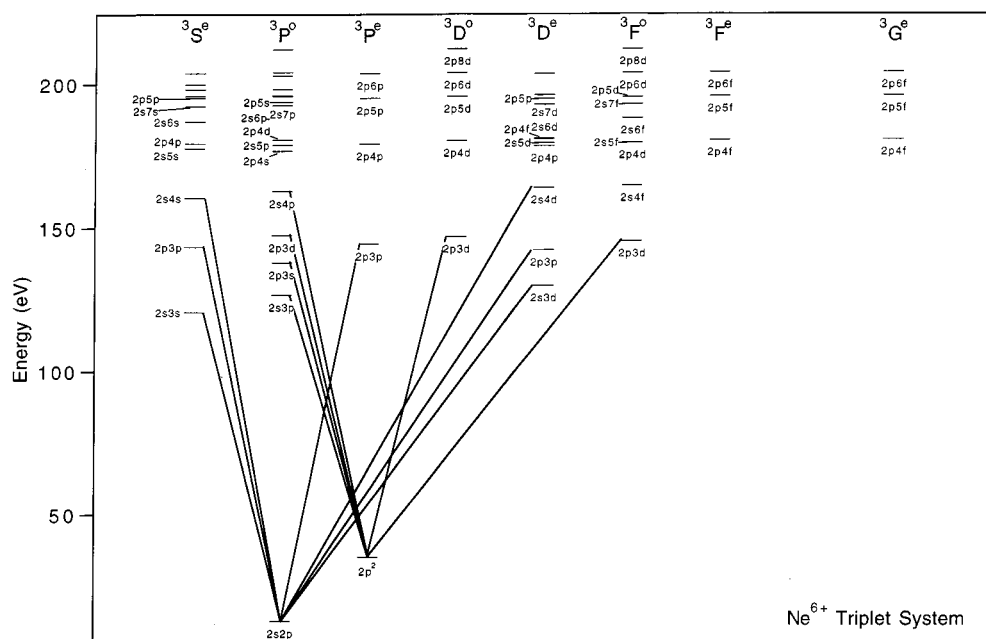


FIG. 6. Grotarian diagram of the lowest (2,3) triplet levels in  $\text{Ne}^{6+}$ . The observed signals are indicated. The observation of triplet signals is discussed separately in the paper.

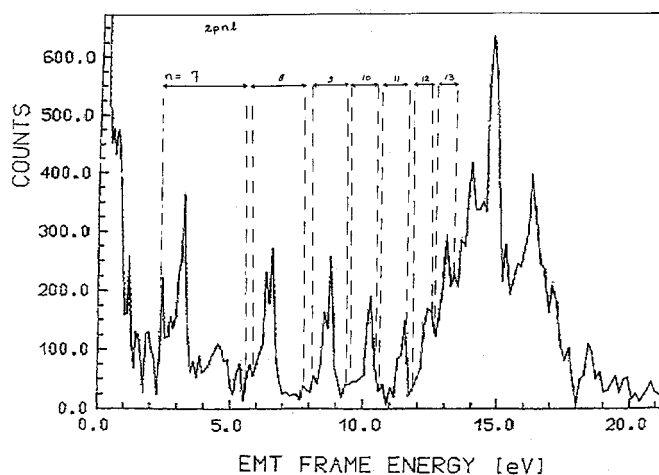


FIG. 7. Blow-up of the low energy part of the Auger electron spectrum. It is indicated for  $n=7-12$ , where the decay of the  $2pnl$  series is to be expected. The array of signals with decreasing intensity fits very well with these expected energy positions. The intensities of the signals decrease as  $n^{-3}$ .

sible to point out joint upper states for the most intense odd (2,3) states. The  $2p3s^3P$  term is populated mainly by  $3s4d^3D$ ,  $3p4p^{1,3}D$ , and  $3p4p^3P$  states. The  $2p3d^1F$  term is mainly populated by  $3d4d^1F$  states. The  $2p3s^3D$  term is mainly populated by  $3d4d^3F$  state, and the  $2s3p^1P$  term is mainly populated by  $3p4p^1P$  states.

The radiative decay channels as discussed above can be compared with complementary information derived from the Auger data. Nonradiative decay from the (3,4) and (3,3) states mentioned above is observed in the Auger data except for the  $3p3d^{1,3}D$  and  $3d4d^3F$  terms. Therefore, these doubly excited states are populated in doubly excited  $\text{Ne}^{6+}$ , either directly or indirectly.

## 2. Nonradiative decay

The most intense Auger electron signals in the 2–13 eV region can be attributed to the decay of  $1s^22pnl$  ( $n=8-12$ ) levels. In Fig. 7 this part of the Auger electron spectrum is presented. Starting at 3.26 eV a series of lines with decreasing intensity is seen. The intensity decreases through the  $n^{-3}$  autoionization probability. This series is disappearing in an intense group of unresolved signals which have energies between 12 and 18 eV. The energy gap between the  $2s$  and  $2p$  continua is 16.1 eV [29]. Therefore, part of the intensity in the 12–18 eV region can originate from the  $2pnl$  series. This intensity also comes from other processes, since the intensity distribution cannot be explained solely by  $2pnl$  decay. In this paper the  $2pnl$  decay only will be discussed up to 13 eV. A detailed discussion of the signals in the 12–18-eV energy region will be presented in a forthcoming paper.

The energies of the  $2pnl$  ( $n=8-13$ ) with  $l \leq 5$  have been calculated with the Cowan programs [28]. The resulting energy regions for the different  $2pnl$  states are indicated in the figure for the different  $n$ -values. The accuracy of the calculated energy regions is decreasing with increasing  $n$ -quantum numbers due to the increasing complexity of the wave functions. It is expected that the low  $l$  levels have larger Auger

rates than the high  $l$  values. This is due to the larger overlap between the electron wave functions with lower  $l$  values. The energy positions, calculated with the Cowan programs suggest that mainly, the  $2pnd$   $^1P$  levels are observed in the Auger spectra. The Auger energies of the  $2pns$ ,  $2pnp$ , and  $2pnd$  levels have been calculated by Mancini and Safronova [30]. Their results are close to the present results but are typically 0.5 eV lower.

There are also signals in the energy region lower than 4.5 eV, possibly due to the decay of (4,4) states to  $3p$  and  $3d$  continua. We present the identifications of these signals in Table VII.

The (3,3) and (3,4) states are most intensively populated. They can decay to the  $2s$  and  $2p$  continua. This can clearly be seen since the signals are divided in two groups divided by 16.1 eV, the distance between the two continua [29]. We have not analyzed the intensity distribution in a quantitative way. The precise intensities in the electron spectra can only be obtained if the line shapes of the individual lines are known. A deconvolution of a spectrum like the one presented here is very difficult. There are many signals and many free parameters in the fitting procedure and we do not expect that a unique fit can be obtained. Interference between overlapping autoionization lines is significant [31,32], and has to be taken into account.

Table IV includes a comparison of the calculated and observed branching ratio for Auger decay to the  $2s$  continuum. The experimental branching ratios are only approximate since we did not deconvolute signals that are overlapping with neighboring signals. There is a fair agreement between the calculations and experiment except for the states that have a calculated branching ratio close to zero. This can be explained by the crude way used to measure the intensities of the lines, causing large absolute errors for weak signals.

We have compared the positions of the observed signals with the PCI shifted theoretical lines. This gives an indication about the accuracy of the calculated lifetimes. It can, however, not be an absolute test, since the position and the lifetime could be wrong both and still agree with the experimentally observed energy. The neglect of the interference limits the accuracy of the conclusions that can be made from the comparison between the theoretical and experimental results. It is however possible to observe that the general agreement is good.

The experimental and theoretical results are summarized in Tables IV, V, and VII. We notice good agreement with previously reported experimental and theoretical results [2,33,34]. The calculated energies of the (3,4) states are generally higher than the ones calculated by Boudjema *et al.*, but fit very well with data from Bachau *et al.* [33]. The results include singlet and triplet states.

The line at 37.3 eV is identified as  $3s3d$   $^3D$ . It is populated in a spin exchange process. For this particular line, its position is close (0.3 eV) to a singlet line and the experimental line width suggests that several levels contribute to the line. Consequently, the identification is optional.

The line at 42.38 eV is identified as the  $3p^2$   $^1D$  term. Its sisterline to the  $2s$  continuum is also observed, in agreement with the calculated transition rates.

The lines at 43.1 and 43.7 eV are well resolved and are far away from calculated singlet signals. They are assigned as

TABLE VI. As in Table V for  $\text{Ne}^{6+}(1s^2 4l4l')$  singlet and triplet states.

State	$E$ (eV)	$E_{\text{c.m.}}$	$\Sigma A_d(s^{-1})$	$\Sigma A_r(s^{-1})$	$\omega_T$	BR $1s^2 2s$	$E_{\text{PCI}}$ (eV)	$E_{\text{expt}}$ (eV)
$4s4s^1S_0$	339.99		2.88+13	1.61+10	5.59-04	0.16	132.7/116.7	116.8/-
$4s4p^3P_0$	340.95		3.26+13	1.59+10	4.89-04	0.08	133.7/117.7	-/117.8
$4s4p^3P_1$	340.96	340.97	3.25+13	1.59+10	4.90-04	0.08	133.7/117.7	-/117.8
$4s4p^3P_2$	340.98		3.25+13	1.59+10	4.89-04	0.08	133.7/117.7	-/117.8
$4s4d^1D_2$	342.04		6.10+13	1.76+10	2.89-04	0.11	134.8/118.7	-/-
$4s4p^1P_1$	342.48		1.09+14	1.80+10	1.66-04	0.08	135.2/119.1	-/119.0
$4s4d^3D_1$	342.70		6.18+13	2.02+10	3.27-04	0	135.4/119.4	-/-
$4s4d^3D_2$	342.70	342.70	6.19+13	2.02+10	3.27-04	0	135.4/119.4	-/-
$4s4d^3D_3$	342.70		6.19+13	2.02+10	3.27-04	0	135.4/119.4	-/-
$4s4f^1F_3$	343.77		2.10+13	1.12+10	5.90-04	0	136.5/120.5	-/120.1
$4s4p^1S_0$	344.54		2.62+14	2.60+10	9.91-05	0.02	137.3/121.1	-/-
$4s4p^1D_2$	344.81		2.81+14	1.97+10	7.02-05	0	137.5/121.3	-/-
$4p4f^1G_4$	344.91		1.35+14	2.15+10	1.59-04	0.03	137.6/121.5	-/-
$4s4f^3F_2$	344.91		1.25+13	1.97+10	1.57-03	0.03	137.6/121.6	-/-
$4s4f^3F_3$	344.92	344.92	1.25+13	1.97+10	1.56-03	0.03	137.6/121.6	-/-
$4s4f^3F_4$	344.92		1.26+13	1.96+10	1.55-03	0.03	137.6/121.6	-/-
$4p4f^3F_4$	344.95		3.02+13	1.88+10	6.21-04	0	137.7/121.7	-/122.0
$4p4d^3P_2$	345.68	345.68	1.02+14	2.59+10	2.53-04	0	138.4/122.4	-/122.0
$4p4d^3P_1$	345.68		6.40+12	2.59+10	4.03-03	0.07	138.4/122.4	-/122.0
$4p4f^3G_3$	345.91		2.77+12	1.22+10	4.37-03	0.11	138.7/122.6	-/-
$4p4f^3G_4$	345.92	345.92	2.77+12	1.21+10	4.35-03	0.11	138.7/122.6	-/-
$4p4f^3G_5$	345.93		2.78+12	1.21+10	4.33-03	0.11	138.7/122.6	-/-
$4p4d^1F_3$	349.10		2.46+14	2.19+10	8.90-05	0	141.8/125.6	-/-
$4p4d^1P_1$	350.15		3.42+14	2.77+10	8.09-05	0	142.9/126.6	-/-
$4p4f^1D_2$	351.59		2.33+14	3.10+10	1.33-04	0	144.3/128.1	-/-
$4p4d^1S_0$	352.97		3.40+12	4.11+10	1.68-02	0.52	145.7/129.7	-/-

$3p3d^3D$  and  $3p3d^3P$  states.

The line at 47.0 eV is identified as a  $3p3d^1F$  state. The sisterline to the  $2s$  continuum is also observed. This is in disagreement with the calculated branching ratio, probably due to the approximative method used to determine the experimental intensities, as described above.

The signals at 49.5 and 50.0 eV are unambiguously attributed to  $3d^2^1D$  and  $3p3d^1D$  states. Previously Boudjema *et al.* [2,3] observed a single signal at 48.5 eV, and assigned it to the  $3d^2^1D$  state. Contrary to these authors, we find that both signals have roughly the same intensity, and we see the decay of these signals to the  $2s$  continuum, in agreement with the calculated branching ratios. The intensity ratios to the  $2s$  and  $2p$  continua are in agreement with the calculated branching ratios.

The signals in the 52–54 eV energy region are not resolved. The assignments in this region are tentative.

The signal at 77.37 eV is the most intense signal in the spectrum. It is attributed to the  $3s4f^1F_3$  state. Its width allows for contribution from the  $3p4s^3P$  and  $3s4f^3F$  terms.

Previous studies reported the absence of the  $3s4s^1D$  decay [2,3]. We do observe the signal at 88.90 eV, close to its calculated value. The state is weakly populated, the intensity is only 25% of the intensity of the  $3s3p^1P$  decay to the  $2s$  continuum at 90 eV.

The signal at 78.4 eV has not been reported before, to our knowledge probably due to blending with the intense  $3p4s$

$^3P$  signal at 77.4 eV. We identified the signal to the decay of the  $3p4s^1P$  state to the  $2p$  continuum. The signal at 79.9 eV is most likely assigned to the  $3p4d^1D_2$  state, very close to its calculated value, but the  $3p4p^3D$  state is calculated at 80.2 eV and cannot be excluded.

The signal at 133.7 eV is intense, but it does not match the signals in the calculated data set. It is probably due to the decay of a  $(3,n)$  state with  $n \geq 5$ . Many of the unidentified signals in Table VII originate from these high states that can not be included in the calculations. In the energy region 115–123 eV our experimental results agree with previous results from Boudjema *et al.* [3].

Most differences between the present measurements and the experimental results from Boudjema *et al.* [2,3] are due to the difference in resolution between the two data sets. The deconvolution procedure used by Boudjema *et al.* should not give different line positions. It is, however, difficult to obtain a unique result using a deconvolution procedure that contains several free parameters. In our opinion a direct identification as presented in this paper is necessary.

A clear general trend with regard to the probability of the population of levels, with a certain angular momentum could not be observed. However, the  $(4,4)$  levels, with a total angular momentum quantum number  $L=1$ , are mostly populated. In the  $(3,4)$  levels it is hard to draw conclusions, but in general  $3l4f$  states are populated. For the  $(3,3)$  levels the  $3s3p^3D$ ,  $3p^2^1D$ ,  $3p3d^1F$ ,  $3d^2^1D$ , and  $3p3d^1P$  states are most intense in the Auger spectra.

#### IV. OBSERVATION OF DECAY FROM TRIPLET STATES

Many of the observed EUV and Auger signals originate from triplet states. However, the radiative signals originate from states in the final decay cascade. Be-like neon is not a pure  $LS$  system. Intercombination transitions are approximately as likely as  $\Delta S=0$  transitions [30]. Many of the observed triplet signals could originate from such processes.

The intense  $2s3d\ 3^D$  signal at 106.10 Å does according to the calculations with the Cowan programs mainly originate from triplet states. We have performed the experiments under single-collision conditions, which implies that the contamination of two-electron transfer processes is only minor. The signal cannot originate from double-collision processes only. We conclude that this particular decay can be explained as due to a spin exchange. This process has been described by Bliman *et al.* [35].

The identification of not completely resolved signals in the Auger spectrum is difficult due to the possible interferences between signals that are close in energy. As described above, deconvolution of the spectra has not been done, and the interferences have not been taken into account. Therefore, only completely resolved signals that are identified as originating from triplet upper levels are considered.

One line in the Auger spectrum can be identified with certainty as originating from a triplet upper state, since it is resolved and not in the vicinity of possible singlet lines according to the calculated data: the decay of the  $3p3d\ 3^D$  state at 59.3 and 43.1 eV to the  $2s$  and  $2p$  continua, respectively. The intensity of this decay is too high to explain it as due to double collisions. It is therefore due to a spin exchange.

#### V. CONCLUSIONS

A comparison has been presented between new atomic structure calculations on doubly excited Be-like neon and experimental data sets consisting of Auger electron and EUV

TABLE VII. Assignment of electron transitions from  $\text{Ne}^{6+}(1s^24l4l')$  states to the  $3p$  and  $d$  continua. The theoretical electron energies uncorrected for the PCI effect and a factor due to the angular dependence of the PCI effect as described in the text are presented to the  $3p$  and  $d$  continua, respectively, together with the experimental values.

Level	$E_{\text{theory}}$ (eV)	$E_{\text{expt}}$
$4p4d^1F_3$	0.6/-	0.6/-
$4p4d^1D$	1.7/0.2	1.9/-
$4p4f^1D$	3.1/1.6	3.1/1.5
$4p4d^1S$	4.5/3.0	4.5/3.1

spectra. The experimental data has been recorded with unprecedented resolution, to our knowledge, and the analysis has been done without deconvolution techniques. The energy positions of the signals were determined. Only the relative intensities of well-resolved signals have been used in the analysis.

In general, a good agreement between the theoretical and experimental data sets has been observed. The final decay path of the TDC is observed directly in the EUV spectra, and from this the feeding decay path can be estimated. Thus information on the TDC decay has been obtained, to our knowledge, for the first time with high-resolution EUV data. The comparison between the Auger electron spectra and the calculated atomic data sets shows good agreement, considering the calculated center of gravity of the multiplets and the observed energy positions of the signals. The branching ratios to the  $2s$  and  $2p$  continua could be determined from the experimental data for some well-separated signals, showing good agreement with the calculated branching ratios. The decay of well-resolved triplet states in the Auger data and the decay of the  $3p3d\ 3^D$  signal in the EUV data is due to a spin exchange.

- 
- [1] M. Barat and P. Roncin, *J. Phys. B* **25**, 2205 (1992).
- [2] M. Boudjema, M. Cornille, J. Dubau, P. Moretto-Capelle, A. Bordenave-Montesquieu, P. Benoit-Cattin, and A. Gleizes, *J. Phys. B* **24**, 1695 (1991).
- [3] M. Boudjema, M. Cornille, J. Dubau, P. Moretto-Capelle, A. Bordenave-Montesquieu, P. Benoit-Cattin, and A. Gleizes, *J. Phys. B* **24**, 1713 (1991).
- [4] F. Folkman, N. H. Eismum, D. Ciric, and A. G. Drentje, *J. Phys. (Paris), Colloq.* **50**, C-1 (1989).
- [5] J. J. Bonnet, A. Fleury, M. Bonnefoy, M. F. Politis, M. Chassevent, S. Bliman, S. Dousson, and D. Hitz, *J. Phys. B* **18**, L23 (1985).
- [6] M. F. Politis, H. Jouin, M. Bonnefoy, J. J. Bonnet, M. Chassevent, A. Fleury, S. Bliman, and C. Harel, *J. Phys. B* **20**, 2267 (1987).
- [7] M. Cornille, J. Dubau, F. Bely-Dubau, S. Bliman, D. Hitz, M. Mayo, J. J. Bonnet, M. Bonnefoy, M. Chassevent, and A. Fleury, *J. Phys. B* **19**, L393 (1986).
- [8] R. A. Phaneuf, *Advanced Sources of Highly Charged Ion Sources*, Experimental Methods in the Physical Sciences Vol. 29A (Academic Press, San Diego, 1995), p. 169.
- [9] A. Bárány, G. Aster, H. Cederquist, H. Danared, S. Hult, P. Hvelplund, A. Johnson, A. Knudsen, L. Liljeby, and K. G. Rensfeldt, *Nucl. Instrum. Methods Phys. Res. B* **9**, 397 (1985).
- [10] A. J. Niehaus, *J. Phys. B* **19**, 2925 (1986).
- [11] H. W. van der Hart, N. Vaeck, and J. E. Hansen, *J. Phys. B* **28**, 2507 (1995).
- [12] P. Roncin, M. N. Gaboriaud, and M. Barat, *Europhys. Lett.* **16**, 551 (1991).
- [13] S. Martin, J. Bernard, A. Denis, J. Désesquelles, L. Chen, and Y. Ouerdane, *Phys. Rev. A* **50**, 2322 (1994).
- [14] H. W. van der Hart, N. Vaeck, and J. E. Hansen, *J. Phys. B* **27**, L395 (1994).
- [15] R. Roncin, M. N. Gaboriaud, M. Barat, A. Bordenave-Montesquieu, P. Moretto-Capelle, M. Benhenni, H. Bachau, and C. Harel, *J. Phys. B* **26**, 4181 (1993).
- [16] J. Nordgren and R. Nyholm, *Nucl. Instrum. Methods Phys. Res. B* **9**, 314 (1985).

- [17] E. B. Saloman, J. S. Pearlman, and B. L. Henke, *Appl. Opt.* **19**, 749 (1980).
- [18] R. L. Kelly, *J. Phys. Chem. Ref. Data* **16**, 155 (1987).
- [19] N. Stolterfoht, A. Itoh, D. Schneider, Th. Schneider, G. Schweitz, H. Platten, G. Nolte, R. Glodde, U. Settner, W. Zeitz, and T. J. M. Zouros, in *International Conference on X-Ray and Inner-Shell Processes in Atoms, Molecules and Solids*, edited by A. Meisel (Leipzig University Press, Leipzig, 1984), p. 1983.
- [20] W. Eisnner, M. Jones, and H. Naussbaumer, *Comput. Phys. Commun.* **8**, 270 (1974).
- [21] J. Dubau and M. Loulergue, *Phys. Scr.* **23**, 136 (1981).
- [22] T. F. R. Group, J. Dubau, and M. Loulergue, *J. Phys. B* **15**, 1007 (1981).
- [23] H. E. Sarah, *Comput. Phys. Commun.* **3**, 256 (1972).
- [24] W. Eisnner and N. V. Seaton, *J. Phys. B* **5**, 2187 (1972).
- [25] R. B. Barker and H. W. Berry, *Phys. Rev.* **15**, 14 (1966).
- [26] P. van der Straten and R. Morgenstern, *Phys. Rev. A* **34**, 4482 (1986).
- [27] M. Barat, M. N. Gaboriaud, L. Guillemot, P. Roncin, H. Laurent, and S. Andriamonje, *J. Phys. B* **20**, 5771 (1987).
- [28] R. D. Cowan, *The Theory of Atomic Structure and Spectra* (University of California Press, Berkeley, 1981).
- [29] S. Bashkin and J. D. Stoner, *Atomic Energy Levels and Grottrian Diagrams*, (North-Holland, Amsterdam, 1975) Vol. 1.
- [30] R. C. Mancini and U. I. Safronova, *J. Phys. B* **28**, 3469 (1995).
- [31] Z. Chen and C. D. Lin, *Phys. Rev. A* **48**, 1298 (1993).
- [32] P. van der Straten and R. Morgenstern, *J. Phys. B* **19**, 1361 (1986).
- [33] H. Bachau, P. Galan, F. Martin, A. Riera, and M. Yanez, *At. Data* **44**, 305 (1990).
- [34] N. Vaeck and J. E. Hansen, *J. Phys. B* **22**, 3137 (1989).
- [35] S. Bliman, R. Bruch, P. L. Altick, D. Schneider, and M. H. Prior, *Phys. Rev. A* **53**, 4176 (1996).